

# Metallicity gradients in Local Universe galaxies: time evolution and effects of radial migration

Laura Magrini<sup>1</sup>, Lodovico Coccatto<sup>2</sup>, Letizia Stanghellini<sup>3</sup>, Viviana Casasola<sup>1</sup>, Daniele Galli<sup>1</sup>

1-INAF -Osservatorio Astrofisico di Arcetri, Largo E. Fermi, 5, I-50125 Firenze, Italy  
2-ESO Karl-Schwarzschild str., 2, 85748 Garching b. Munchen, Germany  
3-National Optical Astronomy Observatory, 950 N. Cherry Avenue, Tucson, AZ 85719, USA  
e-mail: laura@arcetri.astro.it

Received ; accepted

## ABSTRACT

**Context.** Our knowledge of the shape of radial metallicity gradients in disc galaxies has recently improved. Conversely, the understanding of their time evolution is more complex, since it requires analysis of stellar populations with different ages, or systematic studies of galaxies at different redshifts. In the Local Universe, HII regions and planetary nebulae (PNe) are important tools to investigate it.

**Aims.** We present an in-depth study of all nearby spiral galaxies (M33, M31, NGC300, and M81) with *direct*-method nebular abundances of both populations, aiming at studying the evolution of their radial metallicity gradients. For the first time, we also evaluate the radial migration of PN populations.

**Methods.** For the selected galaxies, we analyse HII region and PN properties to: determine whether oxygen in PNe is a reliable tracer for past interstellar medium (ISM) composition; homogenise the published datasets; estimate the migration of the oldest stellar populations; determine the overall chemical enrichment and slope evolution.

**Results.** We confirm that oxygen in PNe is a reliable tracer for the past ISM metallicity. We find that PN gradients are flatter than or equal to those of HII regions. When radial motions are negligible, this result provides a direct measurement of the time evolution of the gradient. For galaxies with dominant radial motions, we provide upper limits on the gradient evolution. Finally, the total metal content increases with time in all target galaxies, with early morphological type having a larger increment  $\Delta(O/H)$  than late-type galaxies.

**Conclusions.** Our findings provide important constraints to discriminate among different galactic evolutionary scenarios, favouring cosmological models with enhanced feedback from supernovae. The advent of extremely large telescopes will allow us to include galaxies in a wider range of morphologies and environments, thus putting firmer constraints to galaxy formation and evolution scenarios.

**Key words.** Interstellar medium (ISM): abundances, HII regions, planetary nebulae – Galaxy: Local Group, evolution, abundances

## 1. Introduction

Spiral galaxies are complex astrophysical objects, showing a non-uniform distribution of metals across their discs. Their radial metallicity distribution, known as the radial metallicity gradient, has been studied for a long time, starting with the pioneering works by Aller (1942) and later by Searle (1971) and Pagel & Edmunds (1981). Nowadays the existence of radial metallicity gradients in spiral galaxies has been tackled in the following cases: individual nearby galaxies, for which *direct*-method measurements are available, i.e., abundance analysis that involves the measurement of the electron temperature and density diagnostic emission lines to characterise the physical conditions of the plasma (see, e.g., Bresolin 2007; Bresolin et al. 2009a; Berg et al. 2012, 2013, 2015); large samples of intermediate distance galaxies, where HII region abundances are derived from the detection of several “strong” emission lines (see, e.g., Sánchez et al. 2014); and high-redshift galaxies (see, e.g., Cresci et al. 2010; Jones et al. 2010, 2013, 2015).

In our Galaxy, metallicity gradients have been estimated using several tracers, from those of relatively young ages, such as OB stars (e.g., Daflon & Cunha 2004), Cepheids

(e.g., Andrievsky et al. 2004; Luck et al. 2006; Yong et al. 2006), HII regions (e.g., Deharveng et al. 2000; Esteban et al. 2005; Rudolph et al. 2006; Balser et al. 2011), to those of intermediate-to-old ages, such as planetary nebulae (e.g., Maciel et al. 2003; Henry et al. 2010; Stanghellini & Haywood 2010) and open clusters (e.g., Friel 1995; Chen et al. 2003; Magrini et al. 2009a).

The general result is that most spiral galaxies show negative radial gradients within their optical radius. In addition, when the observations are deep enough to investigate the outskirts of galaxies, it has been often found that the metallicity tends to reach a plateau: in external galaxies whose gradients are marked by HII regions (Bresolin et al. 2009a; Goddard et al. 2011; Werk et al. 2011; Bresolin et al. 2012) and in our own Galaxy using open clusters (Sestito et al. 2006; Magrini et al. 2009a; Lépine et al. 2011), H II regions (Vilchez & Esteban 1996), and PNe (Maciel & Quireza 1999).<sup>1</sup>

<sup>1</sup> It is worth noting that not all Galactic tracers indicate that the radial metallicity gradients are flat in the outer parts of the galactic disc. For example, Cepheid gradients (Luck et al. 2011; Lemasle et al. 2013) seem to be negative at all radii.

If we focus on regions within the galactic optical radius, where the gradients are clearly negative, the most important open questions are: how was the present time radial gradient established? Was it steeper or flatter in the past? Finding answers to these questions has important implications to our understanding of the processes that lead to the disc formation. In particular, observations allow us to put strong constraints on galactic formation and evolution models (e.g., Pilkington et al. 2012a,b; Gibson et al. 2013; Stinson et al. 2013).

In classical chemical evolution models – in which the cosmological context and the gas and star dynamics are neglected – the different predictions on the time evolution of the radial metallicity gradients depend on the pre-enrichment of the material that formed the primordial disc and whether one assumes a gas density threshold for star formation. A disc formed by pre-enriched gas, and in which a minimum gas density is required to permit the formation of new stars, naturally develops an initial flat metallicity gradient that becomes steeper with time (see, e.g., Chiappini et al. 2001). On the other hand, in models in which the disc is formed by primordial gas and the star formation can proceed at any gas density, the radial metallicity gradient is typically steeper at early times, and flattens as the galaxy evolves (Ferrini et al. 1994; Hou et al. 2000; Mollá & Díaz 2005; Magrini et al. 2009a). Recently, Gibson et al. (2013) have examined the role of energy feedback in shaping the time evolution of abundance gradients within a sub-set of cosmological hydrodynamical disc simulations drawn from the MUGS (McMaster Unbiased Galaxy Simulations; Stinson et al. 2010) and MaGICC (Making Galaxies in a Cosmological Context; Brook et al. 2012) samples. The two sets of simulations adopt two feedback schemes: the conventional one in which about 10-40% of the energy associated with each supernova (SN) is used to heat the ISM, and the enhanced feedback model in which a larger quantity of energy per SN is released, distributed and re-cycled over large scales. The resulting time evolution of the radial gradients is different in the two cases: a strong flattening with time in the former, and relatively flat and temporally invariant abundance gradients in the latter.

In addition, the modelling of the chemical evolution of the galactic disc needs to be combined with dynamics. Both observations and numerical simulations show that stars move from their birth places and migrate throughout the disc during their lifetimes. In our Galaxy, the age-metallicity relationship in the solar neighbourhood puts strong constraints on the presence of radial migration (Edvardsson et al. 1993; Haywood 2008; Schönrich & Binney 2009; Minchev & Famaey 2010): for any given age, there are stars in the solar neighbourhood with a wide range of metallicities and this can only be explained with an exceptionally inhomogeneous ISM or, more likely, with radial migration. From a theoretical point of view, radial stellar migration is related to several processes as the presence of transient spirals (Sellwood & Binney 2002; Roškar et al. 2008), of mergers and perturbations from satellite galaxies and sub-haloes that can induce radial mixing (Quillen et al. 2009), and of a central bar that can stimulate a strong exchange of angular momentum when associated to a spiral structure (Minchev & Famaey 2010; Minchev et al. 2011; Di Matteo et al. 2013; Kubryk et al. 2013). Minchev et al. (2014), by separating the effects of kinematic heating and radial migration, showed the importance of migration needed, especially, to explain the oldest and hottest stellar population.

From an observational point of view, the time evolution of the radial metallicity gradient in nearby external galaxies is well studied with two tracers with similar spectroscopic features, characterising two different epochs in a galaxy lifetime: HII regions and PNe. Studies of PNe and HII region gradients from *direct*-method abundances in M33 (Magrini et al. 2009b, 2010; Bresolin et al. 2010), M81 (Stanghellini et al. 2010, 2014), NGC300 (Bresolin et al. 2009b; Stasińska et al. 2013), and M31 (Zurita & Bresolin 2012) have produced a limited array of results, all indicating gradient invariance, or steepening of the radial O/H gradient with time. These results, summarised in Fig. 9 of Stanghellini et al. (2014), need to be validated by a thorough and homogeneous analysis of all the available data and the gradients recalculated over a common galactocentric scale for all sample galaxies.

The paper is organised as follows: in Section 2 we prove the reliability of PN abundances to investigate the past ISM composition through the invariance of O (at first order) during the lifetime of PN progenitors, while in Section 3 we present our sample of spiral galaxies with the observational datasets. In Section 4 we estimate the effects of radial migration in M31 and M33. In Section 5 we describe the adopted method to homogenise the literature data and to study the time-evolution of radial metallicity gradients. In Section 6 we summarise our results, and in Section 7 we discuss them. We give our summary and conclusions in Section 8.

## 2. Tracing the past: the ISM composition

HII regions are among the best tracers of the present-time composition of the ISM since they are ionised by young massive OB stars that did not have enough time to move from their birth place. On the other hand, PNe are the gaseous remnants of relatively old stellar populations. Before using them as tracers of the past ISM composition, we must consider the nucleosynthesis and mixing processes taking place during their evolution that could modify their composition, and the relevance of their dynamics that could displace them from their initial place of birth (see Section 4).

To obtain a reliable determination of the chemical composition of a nebula from emission lines, we need accurate measurements of the nebula's physical properties, such as electron temperature  $T_e$  and density  $N_e$ . Elemental abundances are often derived from the measurement of collisionally excited lines (CELs), which are very sensitive to  $T_e$ . The latter is derived from the CEL ratios, such as, for instance,  $[\text{OIII}] \lambda 4363 / (\lambda 4959 + \lambda 5007)$ , and  $[\text{NII}] \lambda 5755 / (\lambda 6548 + \lambda 6584)$  nebular-to-auroral line ratios (Osterbrock & Ferland 2006).

An alternative method for nebular abundance determinations is to use the ratio of the intensity of an optical recombination line (ORL) of He or a heavy element, such as O or N, with that of H. The ORLs are less affected by temperature measurement errors since they have a weak dependence on  $T_e$  and  $N_e$ . In regions where both CEL and ORL abundances are available, the ORLs give systematically higher abundances than CELs (e.g., Peimbert et al. 1993; Liu et al. 1995, 2001; Tsamis et al. 2004; García-Rojas & Esteban 2007). This behaviour has been explained, for instance, with the bi-abundance nebular model by Liu et al. (2000) in which the ORLs abundances arise from cold H-deficient small portions of the nebulae, while the strong CELs are emitted predominantly from the warmer ionised gas, and thus are more representative of the global nebular abundance. In addi-

tion, ORLs are much weaker than CELs, and consequently they can be used to measure abundances only in nearby or bright sources. Thus, in most extragalactic studies CELs are adopted to trace the chemical composition, and the total abundance of a given element is computed by summing the abundances of the different ionisation stages of that element.

However, not all the ions are observable in the optical range, and since almost all abundance measurements are based on optical spectroscopy, the ionic sum may underestimate the atomic abundances. The contribution of the unseen ions is usually estimated introducing the so-called ionisation correction factors (ICFs), often based on photoionisation models (Kingsburgh & Barlow 1994; Kwitter & Henry 2001; Delgado-Inglada et al. 2014). In this framework, O is the best measured element in PNe (and HII regions) because: (i) we can directly measure its electron temperatures  $T_e([\text{OIII}])$  from  $[\text{OIII}] \lambda 4363/(\lambda 4959 + \lambda 5007)$  and  $T_e([\text{OII}])$  from  $[\text{OII}] \lambda 7325/(\lambda 3727)$ ; (ii) the transitions relative to the most abundant ionisation stages,  $[\text{OI}]$ ,  $[\text{OII}]$ , and  $[\text{OIII}]$ , are available in the optical range, and consequently no correction for the unseen ionisation stages is needed for the most common low- and intermediate-excitation PNe. In PNe of higher ionisation, the contribution of other O ions may be significant (see Delgado-Inglada et al. 2014, for an updated treatment of the ICF schema).

Before using O/H abundance in PNe as a tracer of the past ISM composition in spiral discs, one needs to prove, from an observational point of view, that O has not been modified during the PN progenitor lifetime in the metallicity range of our interest, typically  $[12+\log(\text{O}/\text{H})] > 8.0$ . The production of O and Ne is indeed dominated by Type II supernovae whose progenitors are massive stars with  $M > 8 M_{\odot}$  (Woosley & Weaver 1995; Herwig 2004; Chieffi & Limongi 2004). From stellar evolution of low- and intermediate-mass stars, we know that the abundance of  $^{16}\text{O}$  can be slightly reduced as a consequence of hot bottom burning in the most massive progenitors. On the other hand, low-mass stars may have a small positive yield of  $^{16}\text{O}$  (Marigo 2001; Karakas & Lattanzio 2007) at low metallicity, while the same effect is negligible for the same stars at solar metallicity. Thus, the O abundance is, in general, expected to be little affected by nucleosynthesis in PN progenitors. The same is true for the abundances of other  $\alpha$ -elements, such as Ne, Ar, and S. A complete review of the sites and processes of production of Ne and O in PNe is presented in Richer & McCall (2008).

From the observational point of view, a study of the relation between Ne and O for a large range of metallicities provides a good way to prove their invariance during the lifetime of PN progenitors. In Fig. 1 we plot O/H vs. Ne/H in a sample of PNe belonging to a variety of galaxies in the Local Group: IC 10 (Magrini & Gonçalves 2009), Sextans A and Sextans B (Magrini et al. 2005), Leo A (van Zee et al. 2006), NGC3109 (Peña et al. 2007), NGC6822 (Hernández-Martínez et al. 2009), NGC205 (Richer & McCall 2008; Gonçalves et al. 2014), NGC185 (Gonçalves et al. 2012), and NGC147 (Gonçalves et al. 2007). The sample also includes three of the spiral galaxies studied in the present paper: M33 (Magrini et al. 2009b; Bresolin et al. 2010), NGC300 (Stasińska et al. 2013), and M81 (Stanghellini et al. 2010).<sup>2</sup> From Fig. 1, we can see that O and Ne abundances are strictly coupled in the majority of PNe, with a slope close to the unity ( $1.03 \pm 0.07$ ). Comparing with the same relationship obtained for

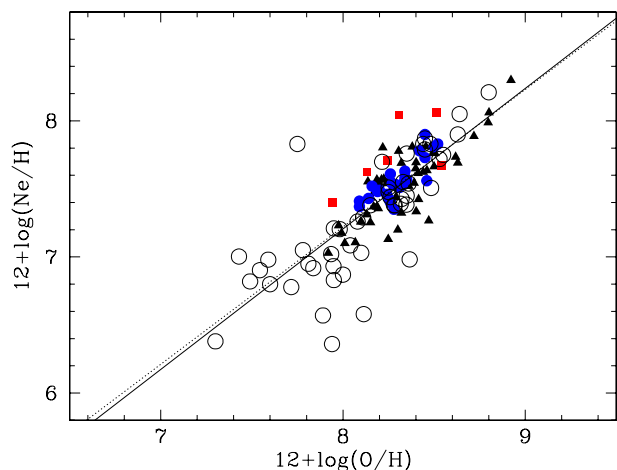


**Fig. 1.** Plot of  $12 + \log(\text{O}/\text{H})$  vs.  $12 + \log(\text{Ne}/\text{H})$  in PNe in M33 (black triangles), M81 (red squares), and NGC300 (blue filled circles). PNe in Local Group dwarf galaxies are shown as empty circles. The continuous line is the linear fit of the abundances of PNe in the whole sample of galaxies, while the dotted line is the fit by Izotov et al. (2006) of star-forming galaxies.

HII regions (with slope 1.01, Izotov et al. 2006), we confirm that the two relations are very similar, with insignificant difference in their slopes, probing that O and Ne in PNe can be used to safely trace the past composition of the ISM.

### 2.1. Dating the PN populations

When using PNe as indicators of the chemical evolution of galaxies, one should be aware that different PN populations probe different epochs, and are subject to different selection effects. Historically, Galactic PNe have been divided into three classes, based on their N and He content, on their location with respect to the Galactic plane, and on their radial velocity (for a summary and references, see Stanghellini & Haywood 2010). Type I PNe are highly enriched in N and He, an occurrence for only the asymptotic giant branch (AGB) stars with an initial mass larger than 2–4.5  $M_{\odot}$  depending on metallicity (e.g., Karakas 2010), corresponding to a very young progenitor population. All non-Type I PNe with high radial velocities are defined as Type III: they are typically located in the Galactic halo, and they are a small minority of Galactic PNe, representing the progeny of the lowest-mass AGB stars. Finally, the most common PNe in the Galaxy are Type II PNe, with intermediate AGB mass progenitors.

However, it is not possible to determine the exact range of progenitor mass for the PNe of each class. From observations, the minimum progenitor mass for a Type I PN is  $\sim 2 M_{\odot}$  (Peimbert & Serrano 1980), and for Type II PN is  $1.2 M_{\odot}$  (Perinotto et al. 2004). From stellar evolution models, the mass range seems to be correlated to metallicity, with the Type I PN mass cutoff (i.e., the critical mass for hot bottom burning) decreasing with metallicity. The population of extragalactic PNe is very similar to that of Galactic PNe, apart from a weak metallicity shift in the limit mass for Type I PN progenitors. The initial mass function (IMF) favours lower mass stars, thus Type I PNe are generally scarce in any galaxy. Furthermore, the evolution of the most massive post-AGB stars is very fast, making the corresponding PN shining for only a few years. Therefore, Type I

<sup>2</sup> For M31 only the O abundance is available in Sanders et al. (2012)

PNe in external galaxies are a very small young population contaminant to the whole PN sample. Type III PNe are typically not observed in spiral galaxies, since they do not trace the spiral arms, where spectroscopic targets are typically chosen. Furthermore, in extragalactic samples one normally observes only the brightest first or second bins of the PN luminosity function (PNLF), which excludes Type III PNe (because they do not reach high luminosity), so most samples are populated by Type II PNe. In the present work we select non-Type I PNe from the original samples, thus most PNe have progenitor mass in the range  $1.2 < M < 2 M_{\odot}$ . This places our PNe at  $\sim 1\text{--}5$  Gyr look-back time (Maraston 1998).

### 3. The sample

There are only four spiral galaxies (other than the Milky Way) in which both HII region and PN abundances are obtained with the *direct*-method. They constitute our sample. The main properties of the four galaxies, including coordinates, distance, optical radius, inclination, position angle, heliocentric systemic velocity and morphology, are listed in Table 1. The references for distance and optical radius are quoted in the Table, while for inclination, position angle, morphology we adopt the values from HyperLeda<sup>3</sup>. For some galaxies, the heliocentric systemic velocity is determined as described in Section 4.1. The quoted value is the average of the velocities obtained from all the individual ellipses. For other galaxies, we the value is obtained from HyperLeda. The sample galaxies have morphological types from very late (NGC300 - Scd) to early type (M81- Sab). M31 and M33 belong to the Local Group: M33 does not have strong interactions with dwarf companions, although it might have had some mutual interaction with M31 in the past (McConnachie et al. 2009; Putman et al. 2009). M31 has several companions that might perturb its dynamics (Chemin et al. 2009; Dierickx et al. 2014). NGC300 is quite isolated, though traditionally considered as a part of the Sculptor group. Finally, M81 is the largest galaxy of the M81 group and it is strongly interacting with its two brightest companions, M82 and NGC3077, located within a short projected distance (60 kpc, Kaufman et al. 1989). The distribution of atomic hydrogen shows several extended tidal streams between M81 and its companions (Yun et al. 1994; Allen et al. 1997), which might be the result of close encounters  $\sim 200\text{--}300$  Myr ago. In addition, M81 presents other peculiarities, as a reduced content of molecular gas with respect to other spiral galaxies (Casasola et al. 2004, 2007).

The PN and HII region populations have been previously studied via medium-resolution optical spectroscopy in all galaxies of our sample. In the following we select abundance determinations via *direct* method for the reasons discussed in Section 2. In order to produce a homogeneous sample of abundances, we selected spectroscopic observations all obtained with comparable telescopes and spectral resolutions. The details of the observations are shown in Table 2, including the reference for the determination of abundances, the telescope name (William Herschel Telescope –WHT; Multiple Mirror Telescope –MMT; Very Large Telescope –VLT) with its diameter, the spectral resolution, the signal-to-noise ratio (SNR) of the faintest auroral lines, and the typical uncertainties on the O abundance. In all datasets, the SNR is adequate for an accurate abundance analysis. In each

galaxy, the uncertainties on O abundances from different literature sources are all comparable.

For M33 we adopt abundances of PNe from Magrini et al. (2009b) (M09) and from Bresolin et al. (2010) (B10), while for HII regions from Magrini et al. (2007, 2010) (M07, M10) and references therein, and B10. For M31, the largest and most recent sample of HII region abundances is computed by using strong-line ratios (Sanders et al. 2012) (S12). For this galaxy we prefer to take advantage of the large sample of Sanders et al. (2012) of HII region abundances and to use the sample (Zurita & Bresolin 2012) (ZB12) with *direct*-method abundances to compute the offset between the *direct* method and the  $N2=[NII]/H\alpha$  calibration. For PNe, there are several studies focussed on different PN populations of M31: PNe in the bulge and disc of M31 (Jacoby & Ciardullo 1999), in the very outer disc (Kwitter et al. 2012; Balick et al. 2013; Corradi et al. 2015), in the Northern Spur and the extension of the Giant Stream (Fang et al. 2013, 2015), and in the whole disc (Sanders et al. 2012). Since we are interested in the behaviour of the gradient within the optical radius, we consider here the abundance determination of Sanders et al. (2012), based on *direct* method, including only PNe that kinematically belong to the disc population, i.e., excluding halo and satellite objects. There are several studies of HII region abundances in M81, some based on strong-line (Garnett & Shields 1987; Bresolin et al. 1999) and others based on the *direct* method (Stanghellini et al. 2010; Patterson et al. 2012; Stanghellini et al. 2014; Arellano-Córdova et al. 2015). We adopt the *direct*-method results from Stanghellini et al. (2010, 2014) (S10, S14), and from Patterson et al. (2012) (P12). In the case of Stanghellini et al. (2014)’s sample, following their analysis, we included only HII regions with uncertainties in O abundance  $< 0.3$  dex in our sample.<sup>4</sup> The only *direct*-method abundance determinations available for M81 PNe are those from Stanghellini et al. (2010), which we use in this paper. Finally for NGC300, the O/H abundances of PNe and of HII regions are from Stasińska et al. (2013) (S13) and Bresolin et al. (2009b) (B09).

For all PN samples, since we are interested in the time evolution of the radial metallicity gradient, we have excluded, whenever possible, Type I PNe, keeping the PNe with the older progenitors.

### 4. Migrating populations

Since PN progenitors have resided in the galaxy for several Gyr, it is essential to quantify their radial migration before proceeding in the analysis of gradient evolution. To do that, we need measurements of their velocity along the line-of-sight and proper motions (the latter being usually not available for extragalactic PNe). Within our galaxy sample, this analysis is possible only for M31 and M33, the galaxies with the largest and most complete sample of PNe with accurate measurements of radial velocities.

<sup>4</sup> We excluded from our sample the abundances of Arellano-Córdova et al. (2015) because of an alternate approach in deriving oxygen abundances, with different temperatures for different ions based on a relation between  $[OIII]$  and  $[NII] T_e$  (e.g., Esteban et al. 2009), with respect to Stanghellini et al. (2010); Patterson et al. (2012); Stanghellini et al. (2014) who used only measured temperatures for all ions. Both approaches are, in principle, correct, but they can produce divergent results when the observational limits of the auroral lines are reached, as in M81.

<sup>3</sup> <http://leda.univ-lyon1.fr/>

**Table 1.** Properties of the galaxy sample

Galaxy	RA	Dec (J2000.0)	Distance (Mpc)	$R_{25}$ (kpc)	Inclination (deg)	PA (deg)	SysVel (km s <sup>-1</sup> )	Morphology
NGC300	00h54m53.48s	+37d41m03.8s	1.88 (Bono et al. 2010)	5.3 (Bresolin et al. 2009b)	48.5	114.3	+165	Scd
M33	01h33m50.9s	+30d39m37s	0.84 (Freedman et al. 2001)	9.0 (Magrini et al. 2007)	55.0	22.7	-185 <sup>a</sup>	Sc
M31	00h42m44.3s	+41d16m09s	0.77 (Tully et al. 2013)	20.6 (Draine et al. 2014)	72.2	35.0	-325 <sup>a</sup>	Sb
M81	09h55M33.2s	+69d03m55s	3.63 (Gerke et al. 2011)	14.6 (Patterson et al. 2012)	62.7	157.0	-38	Sab

Notes – Data with no explicit references are taken from HyperLeda. <sup>a</sup> Determined from the fit in Section 4.1.

**Table 2.** Details of the observations of the considered samples.

Galaxy	Ref.	Telescope	Diameter (m)	Resolution (Å)	SNR	$\delta(O/H)$
M33	Magrini et al. (2007)	WHT	4.2	10	~3-4	0.05-0.10
	Magrini et al. (2009b)	MMT	6.5	5	~10	0.02-0.09
	Magrini et al. (2010)	MMT	6.5	5	~10	0.05-0.12
M31	Bresolin et al. (2010)	Subaru	8.2	4-4.5	≥10	0.08-0.12
	Sanders et al. (2012)	MMT	6.5	5	~10	0.06-0.2
	Zurita & Bresolin (2012)	Keck	10	4.5-5.6	≥10	0.05-0.14
NGC300	Stasińska et al. (2013); Bresolin et al. (2009b)	VLT	8.2	5-10	≤10	0.06-0.15
M81	Stanghellini et al. (2010)	MMT	6.5	5	~5	0.10-0.30
	Stanghellini et al. (2014)	Gemini-N	8.2	5-8	~5	<0.30
	Patterson et al. (2012)	MMT	6.5	5	~5	0.11-0.26

For M31, we combine the datasets of Sanders et al. (2012) and Merrett et al. (2006).

We use only disc PNe, i.e., we remove those PNe that are classified as Hn, halo PNe, or associated to satellites.<sup>5</sup> This results in a sample of 731 PNe with measured radial velocity. For M33, we used the dataset of 140 disc PNe from Ciardullo et al. (2004).

We adopt two complementary approaches that should reveal the effects of different kind of radial motions. In the first approach (Section 4.1), we look for signatures of radial motions in the two-dimensional velocity field of the PN population. In the second one (Section 4.2), we look for PNe that deviate from a simple rotational-disc model, and check if their kinematics is consistent with radial motions. The first method is more sensitive to the presence of group of stars with an average radial component in their velocity vector; the second method is more sensitive to stars with a large radial component in their velocity (and small tangential component), and no net average radial motion.

#### 4.1. Signatures of radial motions on the velocity field

The two-dimensional fields of velocity and velocity dispersion of PNe are recovered from the observations by smoothing the measured velocities  $v(x, y)$  with an adaptive Gaussian kernel along the spatial directions (Peng et al. 2004; Coccato et al. 2009). The size of the kernel represents a compromise between spatial resolution and number of PNe within the kernel that are needed to properly reconstruct the local line-of-sight velocity distribution (LOSVD). The kernel size automatically adapts according to the local PN number density: regions with higher concentration of PNe have smaller kernel size, whereas less populated regions have larger kernel size (see Coccato et al. 2009, for details). The

<sup>5</sup> Sanders et al. (2012) have identified halo PNe in their sample on the basis of their position along the minor axis ( $|Y| > 4$  kpc). Merrett et al. (2006) have identified those PNe that belong to satellites or background galaxies in their sample on the basis of their measured velocities and their proximity to known systems (M32, M110, Andromeda IV and VIII, 2MASX J0039374+420956, and MLAG 0953) (see Section 7 of Merrett et al. (2006) for more details).

two-dimensional fields of the reconstructed velocity  $\langle V \rangle$  and velocity dispersion  $\langle \sigma \rangle$  are shown in Figure 2.

Following the formalism by Teuben (2002), we model the galaxy velocity field  $\langle V \rangle$  with a simple thin disc model that accounts for tangential  $V_{\text{rot}}$  (i.e., rotation) and expansion motions  $V_{\text{exp}}$  (i.e., radial migration, that can be inward or outward),

$$\langle V(x, y) \rangle = V_{\text{sys}} + V_{\text{rot}}(R) \cos \theta \sin i + V_{\text{exp}}(R) \sin \theta \sin i, \quad (1)$$

where  $V_{\text{sys}}$  is the heliocentric systemic velocity,  $(R, \theta)$  are polar coordinates in the plane of the galaxy, and  $(x, y)$  are cartesian coordinates in the plane of the sky ( $\theta = 0$  is aligned with the galaxy photometric major axis and corresponds to positive velocities along the line-of-sight,  $\theta$  increases counter-clockwise). The relationship between the sky and the galaxy planes is given by

$$\tan \theta = \frac{\tan \phi}{\cos i}, \quad R = r \frac{\cos \phi}{\cos \theta}, \quad (2)$$

where  $(r, \phi)$  are polar coordinates in the plane of the sky. Inclinations of  $i = 72^\circ$  and  $i = 55^\circ$  were used for M31 and M33, respectively.

A positive value of  $V_{\text{exp}}$  translates into inward or outward motions depending on which side of the galaxy is the closest to us. This is determined by using the differential reddening of globular clusters. According to this method, the NW side of M31 is the closest to us (Iye & Richter 1985), whereas the SE side of M33 is the closest to us (Iye & Ozawa 1999). Taking into account our sign convention, this leads to have outward motions for positive values of  $V_{\text{exp}}$  in both galaxies.

We fit eq. (1) in several elliptical bins to the reconstructed velocity field computed at the PN position for both galaxies. We kept  $V_{\text{sys}}$  the same for all the bins. The boundaries of the bins are spaced according to an inverse hyperbolic sine function (Lupton et al. 1999). The value of  $R$  associated to a given bin is the median of all the values of  $R$  of all the PNe within that bin. The best fitting semi-major axis profiles of  $V_{\text{rot}}(R)$  and  $V_{\text{exp}}(R)$  are shown in Fig.3. For comparison, we show also the rotation curves of HI gas for M31 (Corbelli et al. 2010) and for M33 (Corbelli & Salucci 2000). Error bars are computed by means of

Monte Carlo simulations in the following way: we constructed 1000 catalogs of simulated PNe that contain as many PNe as observed and located at the same position. The velocity of each simulated PN of coordinates  $(x, y)$  is randomly selected from a Gaussian distribution with mean value  $\langle V(x, y) \rangle$ , and dispersion  $[\Delta V^2(x, y) + \langle \sigma \rangle^2(x, y)]^{1/2}$ , where  $\Delta V(x, y)$  is the measurement error.

The rotation curve of M31 (left panels of Fig. 3) shows a rising profile reaching  $100 \text{ km s}^{-1}$  at 3 kpc ( $0.22^\circ$ ) followed by a plateau starting at  $\sim 6 \text{ kpc}$  ( $0.45^\circ$ ). At larger radii, the scatter in the measured velocity increases. This is reflected by the local peaks in the velocity dispersion maps, and by the presence of kinematic substructures in the velocity map (upper panels of Fig. 2). These features are probably due to the presence of small satellites that contaminated the PN disc population of M31. The majority of these features are offset from the galaxy photometric major axis; this explains the difference between the our PN rotation curve and the one shown by Merrett et al. (2006, their Figure 33), in which only PNe closer than  $0.04^\circ$  to the major axis were considered. The profile of radial motions is consistent with  $0 \text{ km s}^{-1}$  up to  $\sim 7.5 \text{ kpc}$ . For large radii, the contribution of radial motions to the mean velocity field of M31 becomes relevant, reaching  $\sim 100 \text{ km s}^{-1}$  in modulus, despite the observed scatter. There is probably a non negligible contribution from small satellites not identified in Merrett et al. (2006), but it is not possible to disentangle migrating PNe from satellite members with this technique.

In the case of M33, the rotation curve (right panels of Fig.3) matches the rotational velocities of the PNe computed by Ciardullo et al. (2004, their Figure 7a). It reaches a maximum amplitude of about  $\sim 60 \text{ km s}^{-1}$  at  $\sim 5 \text{ kpc}$  and then it remains constant. The profile of radial motion shows large scatter with a weighted average of  $\langle V_{\text{exp}} \rangle = -6 \pm 7 \text{ km s}^{-1}$  (about 6 kpc in 1 Gyr). Its radial velocity profile is consistent with  $0 \text{ km s}^{-1}$  at  $1\sigma$  level for the majority of the bins (at  $3\sigma$  level for all the bins, except for bins 1  $\sim 1 \text{ kpc}$ – and 5  $\sim 5.6 \text{ kpc}$ –) where there is indication of radial inward motions of about  $-12 \text{ km s}^{-1}$ .

Our analysis provides strong indication that there is a significant  $V_{\text{exp}}$  component in the PN system of M31. On the other hand, it provides just a weak indication (at  $1\sigma$  level) that the  $V_{\text{exp}}$  component is present in the 1<sup>st</sup> and 5<sup>th</sup> elliptical bins of M33. In our simple model, we have directly associated  $V_{\text{exp}}$  to radial motions. However, other deviations from circular motions (such as elliptical streaming due to bar-like potential, spiral perturbations, warp of the stellar disc) can mimic the presence of inward or outwards motions (e.g., Wong et al. 2004 and references therein). Therefore, our measurements of the amplitude of radial motions should be considered as upper limits. In the next section, we check whether the best fit  $V_{\text{rot}}$  and  $V_{\text{exp}}$  are consistent with the individual measurements of PN velocities.

#### 4.2. PNe that deviate from a pure rotating disc model

An independent analysis for evaluating radial motion in each elliptical bin is to count PNe that deviate from a pure rotating disc model. According to Section 4.1 we expect to observe deviating PNe outside 7.5 kpc in M31 and on the 1<sup>st</sup> and 5<sup>th</sup> elliptical bins of M33. We fit eq. (1) to the measured PNe velocities  $v(x, y)$  in each elliptical bin setting  $V_{\text{exp}} = 0$ . We then count the number of PNe that deviate more than  $\langle \sigma \rangle(a)$  in each bin, where  $\langle \sigma \rangle(a)$  is the mean velocity dispersion in that bin. We then compare this value with that expected from a pure Gaussian

LOSVD. Results are shown in Tables 3 and 4 for M31 and M33, respectively.

We found that all bins of M31 contain more kinematic outliers than expected by a Gaussian distribution. The measured  $\langle \sigma \rangle$  represents an upper limit to the velocity dispersion of the disc PN population, because of the probable presence of satellites. As a consequence, the estimated number of outliers in Table 3 is a lower limit to the actual value.

In Figure 4 we show the azimuthal distribution of the PNe in M31 for the elliptical bin number 8 (the one with the largest number of outliers compared to the expected number). The corresponding figures for the other bins are shown in Appendix A. The Figure shows that there are plenty of PNe whose line-of-sight velocity is consistent with being on radial migration. They are PNe with nearly 0 velocity, located at the position angles where the rotation is maximum, and PNe with high velocity located at the position angles where the rotation is 0. Indeed, from eq. (1) we expect the radial motions to be minimal (maximal) in correspondence of the position angles where the rotation is maximal (minimal).

In the same Figure, we also show the location of PNe classified as halo or members of satellite systems (which are excluded from the fit). The majority of these PNe are clumped and well separated from the PNe associated to M31. However, there is some overlap between these systems, which can be responsible for some of the radial motions. Also, it is worth noticing that some of the PNe associated to M31 and that deviate from the circular model are clumped together. This indicates that they are kinematically distinct from the PNe in the disc; whether this kinematic separation is entirely due to radial motions or to being part of an (unknown) satellite is beyond the scope of this paper.

In M33, in contrast with Section 4.1, the 1<sup>st</sup> bin does not show more outliers than what expected from a Gaussian distribution. Bin 5 has 9 outliers, whereas 8 are expected. Of those outliers, 8 are located along the photometric major axis, where PNe in radial orbits should have zero velocity projected along the line of sight (LOS, see Eq. (1)). However, those 8 PNe have velocity much higher (in absolute value) than the systemic velocity. Therefore their kinematics is not consistent with radial motions. One PN (in blue in Figure 5) is located along the galaxy photometric minor axis. This is the direction where PNe in radial motions have LOS velocity higher than the systemic velocity. The positive sign of the velocity of that PN is consistent with outward radial motions. However, this is in contrast with what found in section 4.1: radial motions in bin 5, if present, should be directed inwards. Similar arguments hold for bin 4, where an outlier (outside  $3\sigma$ ) is observed along the galaxy photometric minor axis and has a velocity  $75 \text{ km s}^{-1}$ , consistent with outward motions. However, the indication for bin 4<sup>th</sup> – if we ignore the error bar – is that motions are directed inwards.

The two different approaches give weak indications of the presence of radial motions in the PN population of M33, which are in contrast with each other. Even if we consider the upper limits of the radial motions found in our analysis, we can conclude that they do not imply a significant variation for the metallicity gradients of the PN population. In particular, a slight flattening could be produced by a global outward motion, for which we estimate an upper limit of  $\sim 1 \text{ km s}^{-1}$ <sup>6</sup>. This might be a significant amount, if integrated along the whole life-time of a PN progenitor. However, the amount of PNe presently affected by

<sup>6</sup> The upper limit is estimated from  $\langle V_{\text{exp}} \rangle = (-6 \pm 7) \text{ km s}^{-1}$

**Table 3.** Number of PNe in M31 that deviate more than  $1\sigma$  from a pure rotating thin disc model compared with that expected from a pure Gaussian distribution for the elliptical bins. The semi-major axis of each bin is indicated in the second column.

bin	R (kpc)	Outside $1\sigma$	Expected
1	1.87	4	4.0
2	2.31	23	13.0
3	3.61	26	21.1
4	4.63	28	24.1
5	5.87	37	24.4
6	6.36	26	21.1
7	7.30	20	18.5
8	8.30	34	20.5
9	9.75	30	20.5
10	10.71	24	19.5
11	11.24	37	31.0
12	11.45	21	10.2
13	12.28	15	7.9
14	14.90	7	4.0
15	16.08	3	1.7

**Table 4.** Same as Table 3 for M33.

bin	R (kpc)	Outside $1\sigma$	Expected
1	0.80	2	2.6
2	1.24	3	4.0
3	2.03	9	8.6
4	3.12	10	10.2
5	5.03	9	8.3
6	6.77	12	12.5

radial migration does not exceed 7%, as estimated by the number of outliers in Table 3. The dramatic change in the slope of metallicity gradient foreseen by simulations (e.g., Roškar et al. 2008) can be obtained assuming that the migrating stars contribute to  $\approx 50\%$  of the total mass. These numbers are, however, not easy to compare with observations because our measurements describe possible migration at the current time, whereas the quantity in the simulations refer to the galaxy lifetime, and many stars end up on circular orbits after migration. On the other hand, the effect of radial migration is more visible in the scatter of measurements rather than the slope itself (Grand et al. 2015).

In conclusion, our analysis supports the existence of significant radial motions in the PN system of M31. The present-time migration as measured from PNe and, especially, the considerable component of migrating PNe, might be compatible and responsible of the strong variation of the slope of the gradient, from that of PNe to that of HII regions (see Table 5). On the other hand, our analysis does not support the existence of significant radial motions in the PNe system of M33 at present time, with a negligible effect compared to the uncertainties.

## 5. The time-evolution of radial metallicity gradients

In order to determine time-evolution of radial metallicity gradients we proceed with the homogenisation of the literature samples in several ways:

1. *Levelling out the radial scale.* Spiral galaxies have different dimensions, often related also to the morphological type,

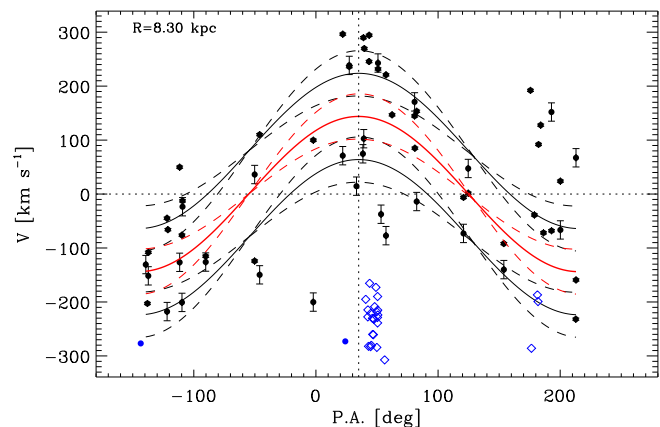


**Fig. 4.** Pure rotation disc model fit to PNe velocities in M31 along the line-of-sight. The plot shows the fit for bin 8. The filled circles are the individual PNe velocities  $v(x, y)$  expressed as function of the position angle on the sky ( $\phi = 0$  in eq. 1 corresponds to  $PA = 35^\circ$ , taken from the HyperLeda database). The red continuous curve represents the best fitting rotation model, the red dashed lines are the model errors, as computed from the Monte Carlo simulations. Continuous black lines indicate the  $\pm\sigma$  level, with the model errors indicated by black dashed lines. Black symbols refer to the analysed PN sample, blue symbols locate the discarded PNe: halo PNe as defined by Sanders et al. (2012, filled blue circles) and satellite PNe as identified by Merrett et al. (2006, open blue diamonds).

with Sa galaxies being more extended than Sd ones. Several studies in the past have shown that the radial metallicity gradients can be related to several galactic properties, such as their morphology (e.g., McCall et al. 1985; Vila-Costas & Edmunds 1992), mass (e.g., Zaritsky et al. 1994; Martin & Roy 1994), presence of a bar (e.g., Zaritsky et al. 1994; Roy 1996), and interaction stage (e.g., Rupke et al. 2010). It has been claimed that the dependence on galaxy properties is evident only if the gradients are expressed in  $\text{dex kpc}^{-1}$  and it disappears when expressed in unit of effective or optical radius. To make sure that the different scale lengths of galactic radii do not produce insignificant correlations with other galactic properties, a good approach is to use, e.g., the optical radius  $R_{25}$  (the 25 mag  $\text{arcsec}^{-2}$  isophotal ratio), the effective or half-light radius  $R_e$ , or the disc scale-length (the scale-length of the exponential describing the profile of the disc),  $R_d$ . To this respect, it is worth noting that the works by Sánchez et al. (2014), Ho et al. (2015), Pilyugin et al. (2014), and (Bresolin & Kennicutt 2015), where radial metallicity gradient slopes are expressed in terms of a reference radius, levelled the differences across galaxies.

The typical gradients of these works range from  $-0.12 \text{ dex}/(R/R_e)$  for Sánchez et al. (2014), to  $-0.39 \pm 0.18 \text{ dex}/(R/R_{25})$  for Ho et al. (2015),  $-0.32 \pm 0.20 \text{ dex}/(R/R_{25})$  for Pilyugin et al. (2014), and  $-0.045 \pm 0.013 \text{ dex}/(R/R_d)$  (O3N2 calibrator) for Bresolin & Kennicutt (2015). Note that Sánchez et al. (2014), Ho et al. (2015) and Bresolin & Kennicutt (2015) express the gradients in different units: for instance, the Sánchez et al. (2014)'s gradient would be  $-0.20 \pm 0.18 \text{ dex}/(R/R_{25})$  if expressed in a  $R_{25}$  scale, as done by Ho et al. (2015) assuming an exponential disc with the typical central surface brightness for normal spirals and the empirical conversion between the different metallicity calibrations (Kewley & Ellison 2008).

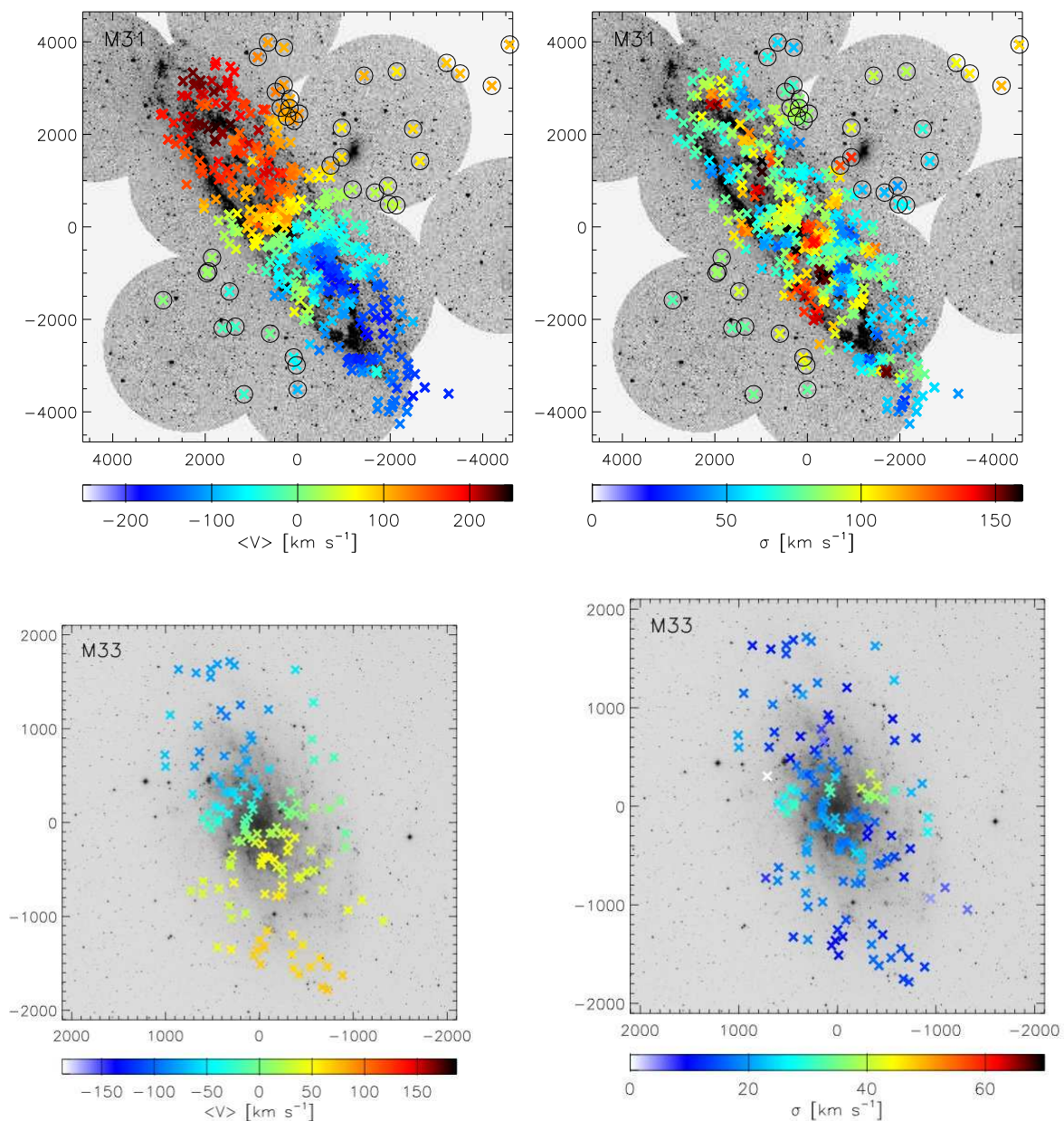


**Fig. 2.** The reconstructed two-dimensional fields of velocity (left panel) and velocity dispersion (right panel) for M31 (upper panels) and M33 (lower panels). Each cross represents the location of a detected PNe, its colour indicates the value of  $\langle V \rangle$  and  $\langle \sigma \rangle$ , as computed via the adaptive Gaussian kernel smoothing in that position. The spatial scale is given in arcsec. North is up, East is left. PNe in M31 that are marked with an open circle were excluded from the analysis of the rotation curve and radial motions.

While all the four examples mentioned above are based on strong-line abundances, there is purpose in comparing the gradients of galaxies of different morphological types based on a common physical scale, as, e.g.,  $R_{25}$ . In this way we can also directly compare same-population gradients of different galaxies.

2. *Binning the data.* Smoothing the data gives in general a better idea of their behaviour. The binning procedure in the analysis of the radial metallicity gradients was performed, e.g., by Maciel & Quireza (1999) in the study of the gradient of PNe and by Huang et al. (2015) in the study of the red clump star gradient. The procedure gives more robustness to the data, removing possible local discrepancies and uncertainties, and de-

fining an average abundance at each galactocentric distance. In addition, it avoids to over-weight some regions in the parameter space where, for several reasons, we might have more data. Each bin is represented by the average abundances of all objects having distances between  $\pm 0.05R/R_{25}$  from the central value. For each galaxy, the different literature sources give comparable errors, thus each data point was equally weighted to produce the final bin value. The error is the standard deviation of the mean.

3. *Comparing common radial bins.* In the CALIFA sample the gradients of many galaxies show evidence of a flattening beyond  $\sim 2$  disc effective radii. This is consistent with several spectroscopic studies of external galaxies (e.g., Bresolin et al.

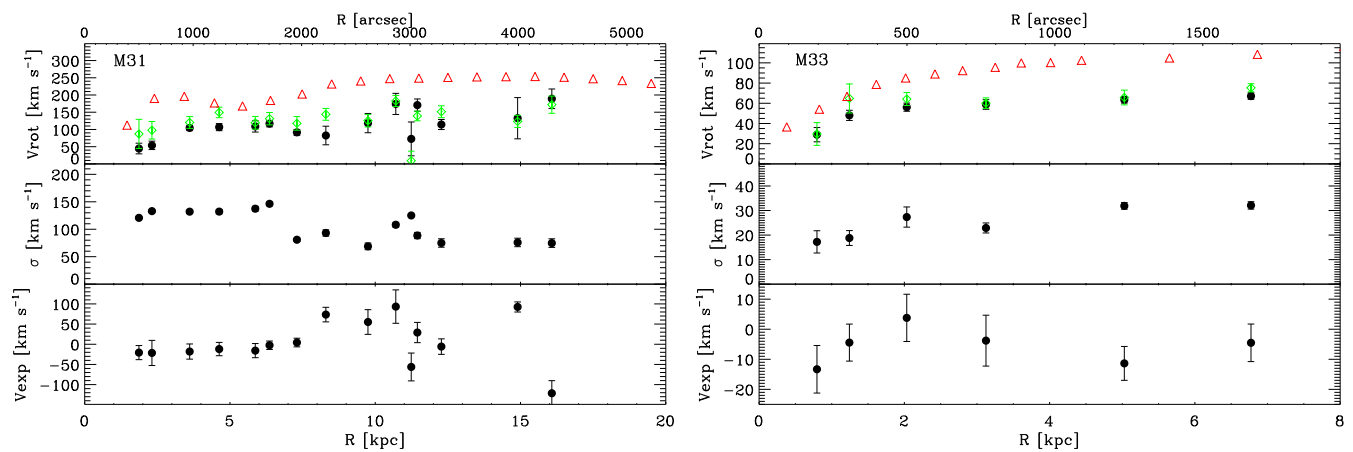


**Fig. 3.** Best fit rotation curve (top), velocity dispersion profile (middle), and radial motions (bottom) of the PN population in M31 (left panel) and M33 (right panel). Black symbols show the results of fitting Eq. (1); green symbols refer to the results when fixing  $V_{\text{exp}} = 0$ ; red triangles show the HI rotation curve as comparison with M31 (Corbelli et al. 2010) and with M33 (Corbelli & Salucci 2000). Positive values of  $V_{\text{exp}}$  correspond to outflowing motions for both galaxies.

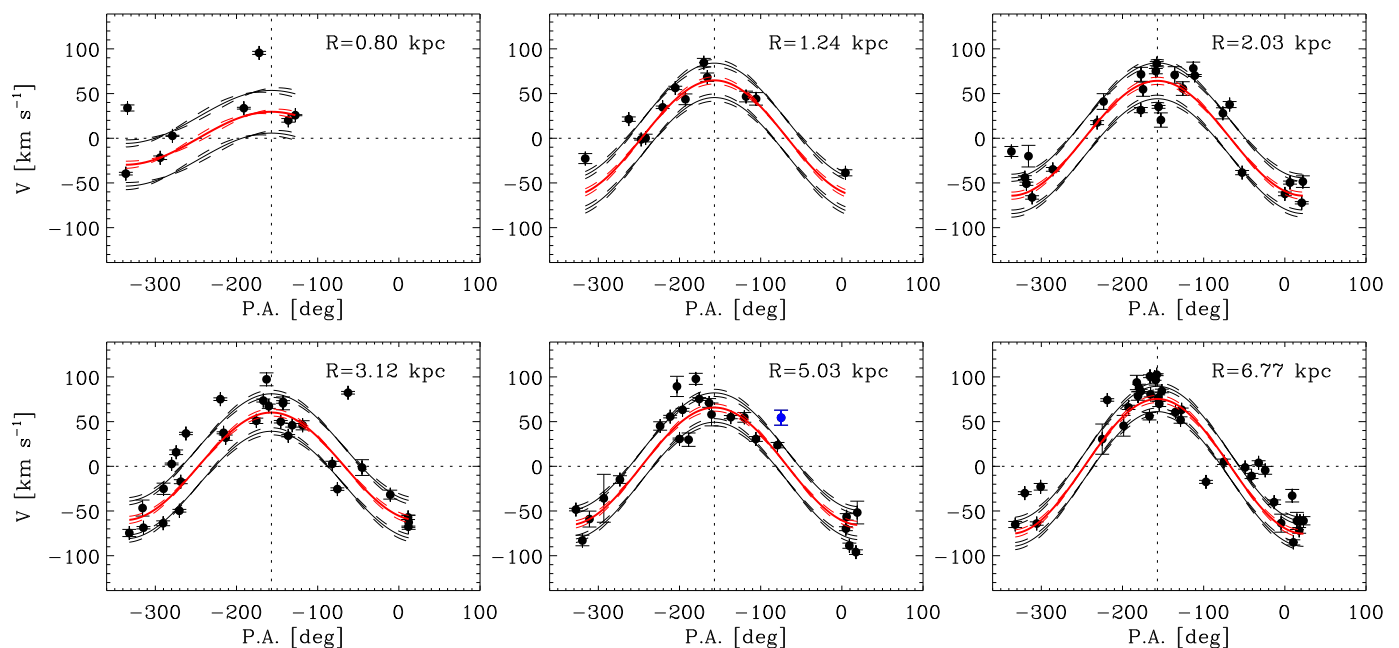


**Fig. 5.** Same as Figure 4, but for all the elliptical bins of M33. The term  $\phi = 0$  in Eq. 1 corresponds to  $PA = -153^\circ$  (taken from the HyperLeda database).

2009a, 2012) and of our own Galaxy (e.g., Magrini et al. 2009a; Lépine et al. 2011; Huang et al. 2015). So, the comparison of different radial regions can lead to misleading results, especially if some of them include very external part of the galactic discs. In the following, we compare similar radial ranges for the H $\alpha$  region and PN population in each galaxy, excluding bins outside  $\sim R_{25}$  where possible changes of slopes might occur.

## 6. Results

### 6.1. Individual galaxies

In Figs. 6, 7, 8, and 9 we show the results of our analysis. In the upper panels of each figure, we show the individual measurements, the gradients obtained from the linear weighted fit

of binned data and the original literature gradients. In the bottom panels, we present the binned abundances with their linear weighted fits.

*NGC300.* Fig. 6 shows the results for NGC300. The two outermost H $\alpha$  region bins have not been included in the fit, since there are no observed PNe in the corresponding bins. Their exclusion explains the small difference with the gradients derived by Stasińska et al. (2013). As already noticed by Stasińska et al. (2013), there is a clear difference in the slopes of the H $\alpha$  region and PN gradients: the gradient in H $\alpha$  regions is steeper than the PN gradient. For this galaxy we cannot evaluate the effect of radial migration, thus the measured steepening with time is an upper limit: the gradient of PNe could have been steeper than the observed one.

*M33.* Fig. 7 shows the results for M33. In this case we excluded on the outermost bin in the PN sample. As already noticed by Magrini et al. (2010), the PN and H II region gradients are indistinguishable within the errors, and present only an offset in metallicity. For M33 the effect of radial migration is negligible, and thus the comparison between the two populations shows the “true” evolution of the gradient, which is null or extremely small.

*M31.* The gradients of M31 are shown in Fig. 8. In the first panel, we show also the *direct*-method abundances of Zurita & Bresolin (2012) for a small number of H II regions. These abundances are much lower than those derived by Sanders et al. (2012) with the N2 indicator. This is a well-known systematic effect due to strong-line vs. *direct* methods (e.g., Kewley & Dopita 2002). However, the slopes of the gradient in the radial region where the two methods overlap are in rough agreement with the gradient from the *direct* method, the latter being slightly steeper. As shown by Stanghellini et al. (2015), the strong-line abundances can indeed give “first order” constraints to galactic evolutionary models, even if more uncertain than the *direct*-method abundances. In the case of M31, the best that we can do is to use the slope derived by the larger sample of Sanders et al. (2012), thus with a better statistics, rescaling the value of the intercept by the average difference of the two bins in common between Zurita & Bresolin (2012) and Sanders et al. (2012). In the bottom panel we compare the PN and H II region gradients. As in the case of NGC300, and even more evidently, the gradient of H II regions is steeper than that of the PN population. However, we recall that for this galaxy we are able to estimate the effects of radial migration. These effects are particularly important at  $\sim 8$  kpc, corresponding to  $\sim 0.4R/R_{25}$  in the  $R_{25}$  scale. This is exactly where we observe an increase in the scatter of the PN abundances and where the radial gradient of PNe show a “jump” of about  $\sim 0.2$  dex. Thus, the steepening with time of the slope of the gradient and the large scatter could be, in part, attributed to the radial migration of its PN population.

*M81.* The results for M81 are shown in Fig. 9. As for the other galaxies examined, the PN gradient is flatter than that of the H II regions, as already noticed by Stanghellini et al. (2014). As for NGC300, no estimate of radial migration for this galaxy are available, thus the steepening with time can be attributed both to migration and to chemical evolution.

## 6.2. General findings

We summarise all gradients in Table 5. Our four galaxies have gradient slopes from the H II region populations ranging from  $-0.22$  dex/( $R/R_{25}$ ) in M33 to  $-0.75$  dex/( $R/R_{25}$ ) in M81; PN gradients are generally flatter, from  $-0.08$  dex/( $R/R_{25}$ ) in M31 to  $-0.46$  dex/( $R/R_{25}$ ) in M81.

The first consideration regards the global enrichment of the galaxies, which can be approximated by the difference in the value of the intercepts in Table 5. The four galaxies have all increased their metallicity content from the epoch of the formation of PN progenitors to the present time. For M31 the intercept computed using the strong-line abundances of Sanders et al. (2012) cannot be directly compared to the PN abundances. Thus we have corrected it using the abundances obtained with the *direct* method by Zurita & Bresolin (2012): the new value gives an almost solar abundance. The metallicity enrichment range from  $+0.05$  dex in M33 to  $+0.32$  dex in M81. The results of the global enrichment are presented in the upper panel of Fig. 10, where

**Table 5.** Gradients of the binned H II regions and PN populations.

Galaxy	Population	Slope dex/( $R/R_{25}$ )	[O/H] Intercept
NGC300	H II	$-0.29 \pm 0.09$	$-0.19 \pm 0.04$
	PN	$-0.10 \pm 0.07$	$-0.32 \pm 0.04$
M33	H II	$-0.22 \pm 0.06$	$-0.27 \pm 0.03$
	PN	$-0.22 \pm 0.05$	$-0.32 \pm 0.03$
M81	H II	$-0.75 \pm 0.10$	$+0.18 \pm 0.04$
	PN	$-0.46 \pm 0.25$	$-0.14 \pm 0.17$
M31	H II	$-0.39 \pm 0.14$	$+0.47 \pm 0.09$
	H II(*)		$-0.01$
	PN	$-0.08 \pm 0.17$	$-0.22 \pm 0.11$

(\*) corrected for *direct* method.

the variations of the intercepts versus the morphological type are shown. Late morphological types have a smaller enrichment while a higher enrichment occurs in early morphological types.

All galaxies of our sample present a small evolution of the gradient slope, that can be a simple uniform metallicity increase as in M33, or a steepening, as in NGC300 and M31. From the present data, there is no observational evidence of gradients flattening with time. In the lower panel of Fig. 10 we present the variation of the gradient slope versus the morphological type. The most significant evolution occurs in early morphological types, while late types tend to have no or smoother evolution. However, we remind that in the case of M31 the radial migration of PNe have an important role in shaping the past gradient.

## 7. Discussion and comparison with models

It is important to compare our results with different kind of galactic chemical evolution models. We have selected two type of models: the classical chemical evolution models, specifically those of the grid of Mollá & Díaz (2005), and the cosmological models of Gibson et al. (2013) with different treatment of the feedback.

In Fig. 11 we compare the gradients of the galaxies with the multi-phase chemical evolution models of Mollá & Díaz (2005) for galaxies with different mass and star formation efficiencies. We excluded M81 because of the strong interaction and environmental effects that prevent to compare with models of isolated galaxies. We selected the most appropriate model on the basis of the total mass of each galaxy, including dark matter, from the grid of Mollá & Díaz (2005), varying the star formation efficiency. The adopted total masses are:  $2.2 \times 10^{11} M_{\odot}$ ,  $4.3 \times 10^{11} M_{\odot}$ , and  $2.0 \times 10^{12} M_{\odot}$  for NGC300, M33, and M31, respectively (Mollá & Díaz 2005).

In the figure we indicate with N the model of Table 1 of Mollá & Díaz (2005) to which we are referring, while the different curves corresponds to different sets of molecular cloud and star formation efficiencies (ranging from 0.007 to 0.95 for the cloud formation efficiency and to  $4 \times 10^{-6}$  to 0.088 for the star formation efficiency).

Left-hand panels show the present-time models and H II region abundances, while right-hand panels show models at roughly the time of the formation of the oldest PN progenitors, i.e., about 5 Gyr ago, and PN abundances. In general, the agreement between the H II region gradients and the present-time modelled gradients is satisfactory for the models with the highest star formation efficiency (from 0.14 to 0.88). Lower star formation

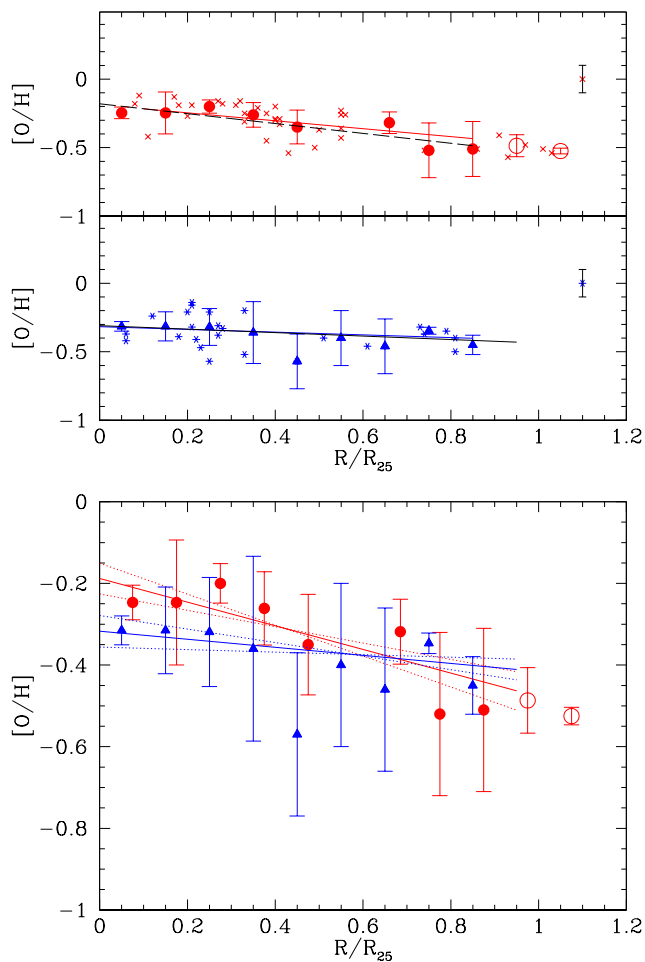


**Fig. 6.** NGC300. *Upper panel:* individual and binned results for HII regions (red circles and crosses for binned and individual results, respectively) and PNe (blue triangles and crosses for binned and individual results, respectively) in NGC300. The O abundances of PNe and of HII regions are from Stasińska et al. (2013) and Bresolin et al. (2009b). The dashed black lines are the gradients of Stasińska et al. (2013). The continuous lines are weighted linear fits computed in the radial regions where both populations are available. The typical errors in O/H for each dataset are shown on the right side of each panel. *Lower panel:* weighted linear fits of PN and HII regions binned metallicities as in the upper panel. Each point corresponds to the average metallicity of the PN or HII region population in a radial bin of  $0.1R/R_{25}$ . Empty symbols are for radial positions outside  $R_{25}$  or for populations that have no correspondence in the other sample (excluded from the fits). Dotted lines indicate the errors on the slopes and on the intercepts.

efficiencies (from  $0.05$  to  $4 \times 10^{-6}$ ) produce gradients with shorter scale-lengths. For NGC300 and M33, the observed PN gradients and the models are quite close, whereas for M31 the result from the old population is flatter than any modelled galaxy. In this galaxy, radial migration is important and can contribute to the flattening of the PN gradient.

An interesting point to be noticed from Fig. 11 is that modelled radial metallicity gradient, and likely the *real* gradients, are well away from being approximated by a single slope. Probably, our simplistic assumption of a single slope gradient hides a more complex time evolution of the metallicity distribution, in which, for instance, inner and outer regions do not evolve at the same rate.

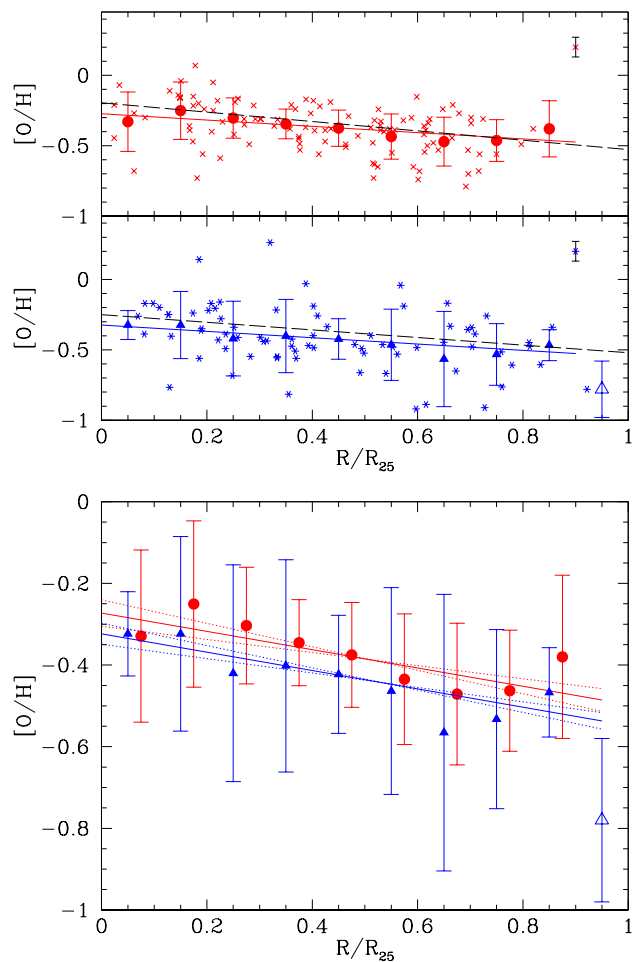


**Fig. 7.** M33. *Upper panel:* individual and binned results for HII regions (upper panel) and PNe (lower panel) in M33. The O abundances of PNe are from Magrini et al. (2009b) and Bresolin et al. (2010) (blue stars) and of HII regions from Magrini et al. (2007, 2010) and references therein, and Bresolin et al. (2010) (red crosses). The continuous black lines are the gradient of Magrini et al. (2010) for HII regions (their whole sample) and the non-Type I PN sample of Magrini et al. (2009b), in the upper and lower panels, respectively. *Lower panel:* weighted linear fits of PN and HII region binned metallicities. Symbols and curves as in Fig. 6.

In Fig. 12, we compare the cosmological models of Gibson et al. (2013) with different treatment of the feedback, "enhanced" and "conservative" feedbacks, with our gradient slopes from HII regions and PNe. The models are built to reproduce the present-time gradient of a Milky-Way-like galaxy, therefore it is not surprising that the agreement with the HII regions gradient is good. The range of values for our HII region gradients indicates the dependence on the morphological type when the gradients are expressed in terms of  $\text{dex kpc}^{-1}$ . On the other hand, the gradients traced by PNe put important constraints on the models: the current data certainly favour a smooth evolution of the gradient and are not consistent with a flatter gradient in the past in the time lapse (and redshift interval) constrained by PNe. Comparing the data with the two sets of models, "enhanced" and "conservative" feedbacks, at the epoch of birth of PNe we can discern a better agreement with the first class of models, in which the energy of SNe is widely redistributed. All

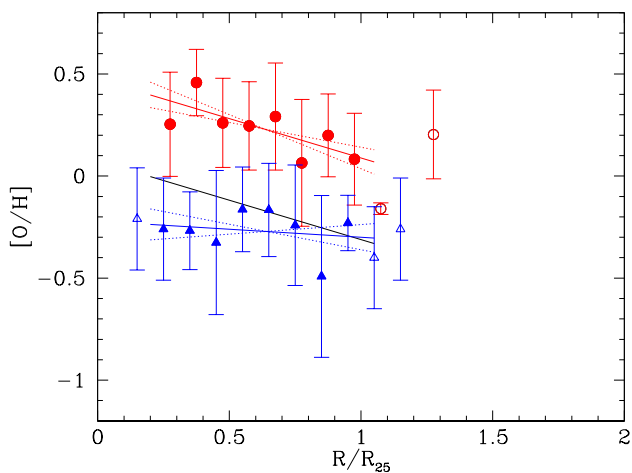
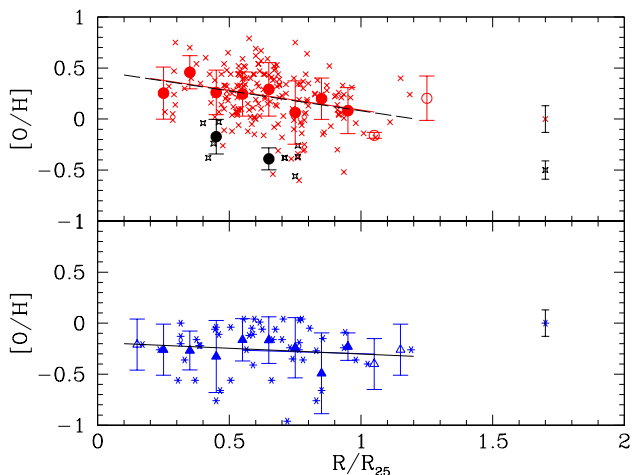


**Fig. 8.** M31. *Upper panel:* individual and binned results for HII regions (upper panel) and PNe (lower panel) in M31. The O abundances of PNe are from Sanders et al. (2012) (blue stars) and of HII regions from Zurita & Bresolin (2012) (black empty stars) and from Sanders et al. (2012) (red crosses). The black filled circles are the HII regions binned metallicities of Zurita & Bresolin (2012). *Lower panel:* weighted linear fits of PN and HII region binned metallicities. Symbols and curves as in Fig. 6.

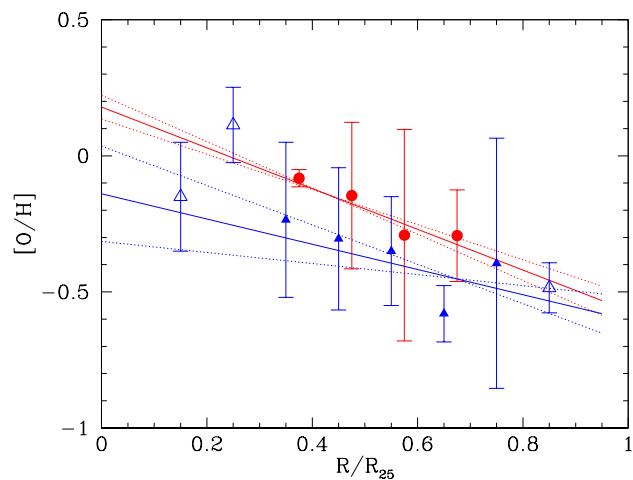
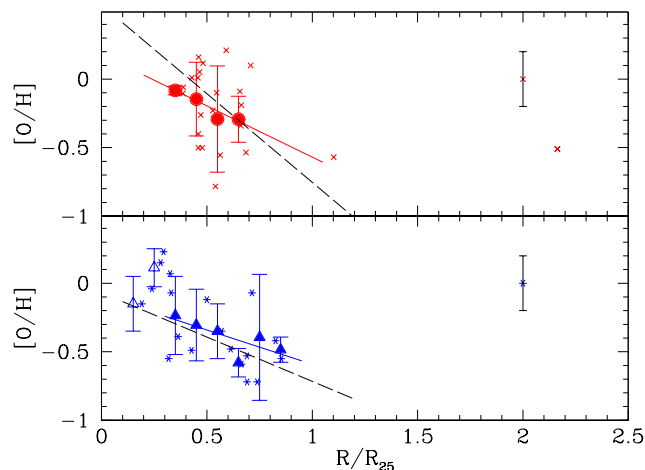


**Fig. 9.** M81. *Upper panel:* individual and binned results for HII regions (upper panel) and PNe (lower panel). The O abundances of PNe are taken from Stanghellini et al. (2010) and those of HII regions from Stanghellini et al. (2010, 2014) and Patterson et al. (2012). The continuous black lines are the gradient of Stanghellini et al. (2014) for PNe and that of Stanghellini et al. (2014) for HII regions. *Lower panel:* weighted linear fits of PN and HII region binned metallicities. Symbols and curves as in Fig. 6.

PN gradients in this plot have been placed at 5 Gyr, corresponding to progenitor mass at turnoff of  $1.2 M_{\odot}$  (Maraston 1998). This is the lower limit of masses of Type II PNe, favoured by the IMF, but may not strictly represent the progenitor mass/look-back time for all PN within each sample. Each PN sample can be contaminated by a few Type III PNe, which would probe higher redshifts ( $0.5 < z < 8$ ). On the other hand, we have excluded Type I PNe, as discussed above. With cosmological parameters  $H_0 = 67.04 \text{ km s}^{-1} \text{ Mpc}^{-1}$ ,  $\Omega_m = 0.3183$ ,  $\Omega_{\Lambda} = 0.6817$ , this look-back time corresponds to a redshift of  $z \approx 0.5$ .

It is clear from the plot that extragalactic PNe cannot trace the most remote past of galaxies, probing the epochs where the two scenarios mostly differ. For example, one of the models with more conservative feedback (the dashed magenta curve in Fig. 12) is still consistent, within the errors, with the observational constraints from PNe. It is worth noting that Type III Galactic PNe probe look-back time up to 8 Gyr, and that the Type III PN gradient observed in the Galaxy Stanghellini & Haywood (2010) also agrees with the enhanced feedback models (see

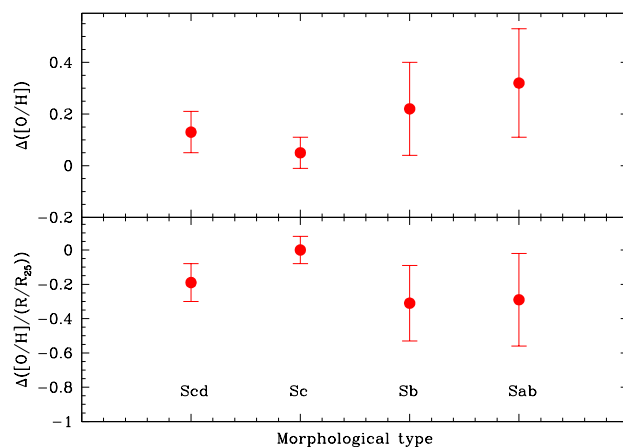


**Fig. 10.** Global enrichment (upper panel) and variation of the slope of the metallicity gradient (lower panel) as a function of the morphological type.

Gibson et al. 2013). Nonetheless, the Galactic PN gradient suffers from uncertainties in the distance scale, which make this constraint not very strong. For these reasons, Local Universe constraints need to be complemented with high-redshift observations, as those of Cresci et al. (2010), Jones et al. (2010, 2013, 2015), and Yuan et al. (2011), that are able to shed light to the very early phases of disc evolution.

## 8. Summary

In the present work, we have analysed in a homogeneous way the literature data on *direct*-method abundances of H II regions and PNe in four nearby disc galaxies: NGC300, M33, M31, and M81. The abundances of H II regions in M31 are an important exception, since only very few regions have *direct*-method abundances (Zurita & Bresolin 2012), while a large sample with abundances derived with strong lines is available (Sanders et al. 2012). In this case, we take advantage of the large sample of Sanders et al. (2012) and we use the sample (Zurita & Bresolin 2012) to compute the offset between the *direct* method and the strong-line calibration.

The analysed galaxies belong to different morphological types and allow us to study the time evolution of the metallicity enrichment and of the gradient as a function of galaxy morphology assuming that no correction is needed for the slope for stellar migration. To properly exploit PNe as tracers of the past composition of the ISM, we have proved that their O abundances are unchanged at first order during the progenitor stellar evolution. Moreover, we have estimated the amplitude of radial migration of the two galaxies in the sample with measured radial velocities. In the case of M33, we have shown that the effects of radial migration on the metallicity gradients are negligible. In the case of M31, the effects of radial migration in the PN velocity field is non-negligible, and could have affected significantly the radial metallicity gradient in the last few Gyr.

Using H II regions and PNe as tracers of the time evolution of the metallicity distribution in disc galaxies, we have found that: (i) all galaxies are subject to a global oxygen enrichment with time, higher for earlier type spirals (Sa-Sb); (ii) on average, the O/H gradients of the older population are equal to or flatter than those of H II regions. While steeper O/H gradients for young populations have been noted before in spiral galaxies from *direct* abundances of PNe and H II regions (Magrini et al. 2009b; Stasińska et al. 2013; Stanghellini et al. 2014), we confirm this trend when galaxies are studied in a comparable radial domain and metallicity binning. (iii) Our kinematical study of PNe in M33 and in M31 finds that radial migration can contribute to the observed flattening, especially in the case of M 31. The undisturbed PN population of M33 allows us to better constrain the time evolution of the radial gradient.

Our radial gradients and their time-evolution are compared with classical and cosmological chemical evolution models. They are found to be in good agreement with the multiphase chemical evolution models by Mollá & Díaz (2005). Using our results as constraints to the cosmological models of galaxy evolution of Gibson et al. (2013), we find that, in the redshift range sampled by H II regions and PNe, models with enhanced SN feedback are favoured.

With the current technology, the realm of star-forming galaxies, where the time evolution of the metallicity gradient evolution can be obtained from *direct*-method abundances, is limited. By setting a limit from the PNe studied so far and reasonable

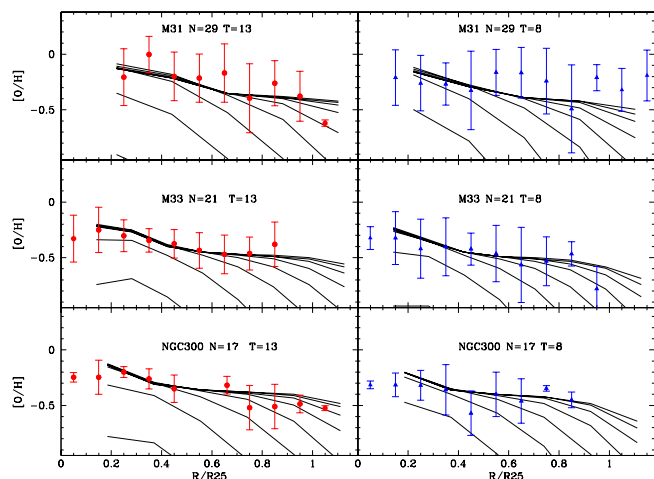


**Fig. 11.** Comparison with the multi-phase chemical evolution models of Mollá & Díaz (2005) for galaxies with different mass and star formation efficiencies. The panels to the left present the models at the present time ( $T = 13$  Gyr), while the panels to the right show the models at the epoch of PN formation ( $T = 8$  Gyr). Each curve is for a given star formation efficiency. For each galaxy we chose the most appropriate mass distribution indicated by N in the plots, where N is the designation of the model in Table 1 of Mollá & Díaz (2005)

observability in a few 8m-class telescope nights, we expect to enlarge our sample by few more galaxies. This would allow to refine the evolutionary trends shown in Fig. 12. We also expect to acquire in the near future deeper spectra of the current galaxies, to better characterise their PN and H II region populations, as for instance in M31, and possibly to reveal older PN populations. However, the strongest constraints to the galactic evolutionary models are expected to come from either a better determination of the distance scale for Galactic PNe, to which the Gaia satellite will contribute, from abundance studies of high-redshift galaxies, and from the future 30m-class telescopes. The latter will favour both better characterisation of PNe and H II regions in the nearby galaxies with optical multi-object spectroscopy and abundances of redshifted galaxies with infrared integral field unit spectroscopy.

**Acknowledgements.** The authors are very grateful to the referee for her/his constructive report that improved the quality and presentation of the paper. This research has made use of the NASA/IPAC Extragalactic Database (NED) which is operated by the Jet Propulsion Laboratory, California Institute of Technology, under contract with the National Aeronautics and Space Administration. We acknowledge the usage of the HyperLeda database. V.C. acknowledges DustPedia, a collaborative focused research project supported by the European Union under the Seventh Framework Programme (2007-2013) call (proposal no. 606824). The participating institutions are: Cardiff University, UK; National Observatory of Athens, Greece; Ghent University, Belgium; Université Paris Sud, France; National Institute for Astrophysics, Italy and CEA (Paris), France.

## References

- Allen, R. J., Knapen, J. H., Bohlin, R., & Stecher, T. P. 1997, *ApJ*, 487, 171
- Aller, L. H. 1942, *ApJ*, 95, 52
- Andrievsky, S. M., Luck, R. E., Martin, P., & Lépine, J. R. D. 2004, *A&A*, 413, 159
- Arellano-Córdova, K. Z., Rodríguez, M., Mayya, Y. D., & Rosa-González, D. 2015, arXiv:1510.07757

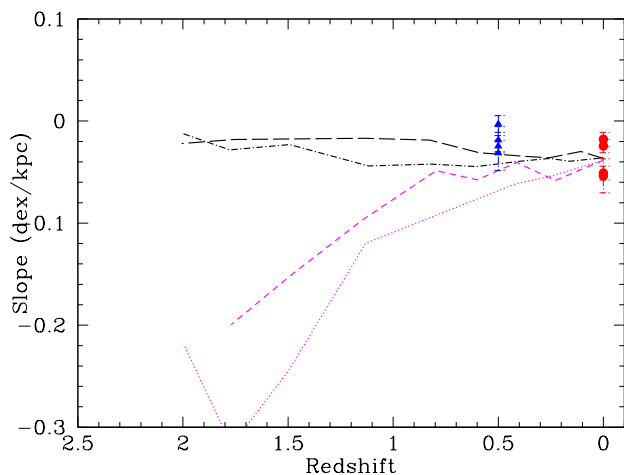


**Fig. 12.** Comparison of the redshift evolution of the gradient with the chemical evolution models of Gibson et al. (2013): black (dashed and dot-dashed) lines are models with enhanced feedback from SNe, magenta (short-dashed and dotted) lines are models with normal feedback. Red circles and blue triangles show the slopes of the gradients from HII regions and PNe with  $1.2 M_{\odot}$  progenitors, respectively. Note that in this plot the slopes are expressed in dex/kpc to be compared with the models of Gibson et al. (2013).

- Balick, B., Kwitter, K. B., Corradi, R. L. M., & Henry, R. B. C. 2013, *ApJ*, 774, 3
- Balsler, D. S., Rood, R. T., Bania, T. M., & Anderson, L. D. 2011, *ApJ*, 738, 27
- Berg, D. A., Skillman, E. D., Marble, A. R., et al. 2012, *ApJ*, 754, 98
- Berg, D. A., Skillman, E. D., Garnett, D. R., et al. 2013, *ApJ*, 775, 128
- Berg, D. A., Skillman, E. D., Croxall, K. V., et al. 2015, *ApJ*, 806, 16
- Bono, G., Caputo, F., Marconi, M., & Musella, I. 2010, *ApJ*, 715, 277
- Bresolin, F., & Kennicutt, R. C. 2015, *MNRAS*, 454, 3664
- Bresolin, F., Kennicutt, R. C., Jr., & Garnett, D. R. 1999, *ApJ*, 510, 104
- Bresolin, F. 2007, *ApJ*, 656, 186
- Bresolin, F., Gieren, W., Kudritzki, R.-P., et al. 2009a, *ApJ*, 700, 309
- Bresolin, F., Gieren, W., Kudritzki, R.-P., et al. 2009b, *ApJ*, 700, 309
- Bresolin, F., Stasińska, G., Vílchez, J. M., Simon, J. D., & Rosolowsky, E. 2010, *MNRAS*, 404, 1679
- Bresolin, F., Kennicutt, R. C., & Ryan-Weber, E. 2012, *ApJ*, 750, 122
- Brook, C. B., Stinson, G., Gibson, B. K., Wadsley, J., & Quinn, T. 2012, *MNRAS*, 424, 1275
- Casasola, V., Bettoni, D., & Galletta, G. 2004, *A&A*, 422, 941
- Casasola, V., Combes, F., Bettoni, D., & Galletta, G. 2007, *A&A*, 473, 771
- Chemin, L., Carignan, C., & Foster, T. 2009, *ApJ*, 705, 1395
- Chen, L., Hou, J. L., & Wang, J. J. 2003, *AJ*, 125, 1397
- Chiappini, C., Matteucci, F., & Romano, D. 2001, *ApJ*, 554, 1044
- Chieffi, A., & Limongi, M. 2004, *ApJ*, 608, 405
- Ciardullo, R., Durrell, P. R., Laychak, M. B., et al. 2004, *ApJ*, 614, 167
- Coccatto, L., Gerhard, O., Arnaboldi, M., et al. 2009, *MNRAS*, 394, 1249
- Corbelli, E., Salucci, P. 2000 *MNRAS*, 311, 441
- Corbelli, E., Lorenzoni, S., Walterbos, R., Braun, R., & Thilker, D. 2010, *A&A*, 511, A89
- Corradi, R. L. M., Kwitter, K. B., Balick, B., Henry, R. B. C., & Hensley, K. 2015, *ApJ*, 807, 181
- Cresci, G., Mannucci, F., Maiolino, R., et al. 2010, *Nature*, 467, 811
- Dafon, S., & Cunha, K. 2004, *ApJ*, 617, 1115
- Deharveng, L., Peña, M., Caplan, J., & Costero, R. 2000, *MNRAS*, 311, 329
- Delgado-Inglada, G., Morisset, C., & Stasińska, G. 2014, *MNRAS*, 440, 536
- Dierickx, M., Blecha, L., & Loeb, A. 2014, *ApJ*, 788, L38
- Di Matteo, P., Haywood, M., Combes, F., Semelin, B., & Snaith, O. N. 2013, *A&A*, 553, A102
- Draine, B. T., Aniano, G., Krause, O., et al. 2014, *ApJ*, 780, 172
- Edvardsson, B., Andersen, J., Gustafsson, B., et al. 1993, *A&A*, 275, 101
- Esteban, C., García-Rojas, J., Peimbert, M., et al. 2005, *ApJ*, 618, L95
- Esteban, C., Bresolin, F., Peimbert, M., et al. 2009, *ApJ*, 700, 654
- Fang, X., Zhang, Y., García-Benito, R., Liu, X.-W., & Yuan, H.-B. 2013, *ApJ*, 774, 138
- Fang, X., García-Benito, R., Guerrero, M. A., et al. 2015, arXiv:1511.02788
- Ferrini, F., Molla, M., Pardi, M. C., & Diaz, A. I. 1994, *ApJ*, 427, 745
- Freedman, W. L., Madore, B. F., Gibson, B. K., et al. 2001, *ApJ*, 553, 47
- Friel, E. D. 1995, *ARA&A*, 33, 381
- García-Rojas, J., & Esteban, C. 2007, *ApJ*, 670, 457
- Garnett, D. R., & Shields, G. A. 1987, *ApJ*, 317, 82
- Gerke, J. R., Kochanek, C. S., Prieto, J. L., Stanek, K. Z., & Macri, L. M. 2011, *ApJ*, 743, 176
- Gibson, B. K., Pilkington, K., Brook, C. B., Stinson, G. S., & Bailin, J. 2013, *A&A*, 554, A47
- Goddard, Q. E., Bresolin, F., Kennicutt, R. C., Ryan-Weber, E. V., & Rosales-Ortega, F. F. 2011, *MNRAS*, 412, 1246
- Gonçalves, D. R., Magrini, L., Leisy, P., & Corradi, R. L. M. 2007, *MNRAS*, 375, 715
- Gonçalves, D. R., Magrini, L., Martins, L. P., Teodorescu, A. M., & Quireza, C. 2012, *MNRAS*, 419, 854
- Gonçalves, D. R., Magrini, L., Teodorescu, A. M., & Carneiro, C. M. 2014, *MNRAS*, 444, 1705
- Grand, R. J. J., Kawata, D., & Cropper, M. 2015, *MNRAS*, 447, 4018
- Haywood, M. 2008, *MNRAS*, 388, 1175
- Hernández-Martínez, L., Peña, M., Carigi, L., & García-Rojas, J. 2009, *A&A*, 505, 1027
- Henry, R. B. C., Kwitter, K. B., Jaskot, A. E., et al. 2010, *ApJ*, 724, 748
- Herwig, F. 2004, *ApJS*, 155, 651
- Ho, I.-T., Kudritzki, R.-P., Kewley, L. J., et al. 2015, *MNRAS*, 448, 2030
- Hou, J. L., Prantzos, N., & Boissier, S. 2000, *A&A*, 362, 921
- Huang, Y., Liu, X.-W., Zhang, H.-W., et al. 2015, *Research in Astronomy and Astrophysics*, 15, 1240
- Iye, M., & Richter, O.-G. 1985, *A&A*, 144, 471
- Iye, M., & Ozawa, T. 1999, *Galaxy Dynamics - A Rutgers Symposium*, 182,
- Izotov, Y. I., Stasińska, G., Meynet, G., Guseva, N. G., & Thuan, T. X. 2006, *A&A*, 448, 955
- Jacoby, G. H., & Ciardullo, R. 1999, *ApJ*, 515, 169
- Jones, T., Ellis, R., Jullo, E., & Richard, J. 2010, *ApJ*, 725, L176
- Jones, T., Ellis, R. S., Richard, J., & Jullo, E. 2013, *ApJ*, 765, 48
- Jones, T., Wang, X., Schmidt, K. B., et al. 2015, *AJ*, 149, 107
- Karakas, A. I. 2010, *MNRAS*, 403, 1413
- Karakas, A., & Lattanzio, J. C. 2007, *PASA*, 24, 103
- Kaufman, M., Bash, F. N., Hine, B., et al. 1989, *ApJ*, 345, 674
- Kewley, L. J., & Dopita, M. A. 2002, *ApJS*, 142, 35
- Kewley, L. J., & Ellison, S. L. 2008, *ApJ*, 681, 1183
- Kingsburgh, R. L., & Barlow, M. J. 1994, *MNRAS*, 271, 257
- Kubryk, M., Prantzos, N., & Athanassoula, E. 2013, *MNRAS*, 436, 1479
- Kwitter, K. B., & Henry, R. B. C. 2001, *ApJ*, 562, 804
- Kwitter, K. B., Lehman, E. M. M., Balick, B., & Henry, R. B. C. 2012, *ApJ*, 753, 12
- Lépine, J. R. D., Cruz, P., Scarano, S., Jr., et al. 2011, *MNRAS*, 417, 698
- Liu, X.-W., Storey, P. J., Barlow, M. J., & Clegg, R. E. S. 1995, *MNRAS*, 272, 369
- Liu, X.-W., Storey, P. J., Barlow, M. J., et al. 2000, *MNRAS*, 312, 585
- Liu, X.-W., Luo, S.-G., Barlow, M. J., Danziger, I. J., & Storey, P. J. 2001, *MNRAS*, 327, 141
- Lemasle, B., François, P., Genovali, K., et al. 2013, *A&A*, 558, A31
- Luck, R. E., Kovtyukh, V. V., & Andrievsky, S. M. 2006, *AJ*, 132, 902
- Luck, R. E., Andrievsky, S. M., Kovtyukh, V. V., Gieren, W., & Graczyk, D. 2011, *AJ*, 142, 51
- Lupton, R. H., Gunn, J. E., & Szalay, A. S. 1999, *AJ*, 118, 1406
- Maciel, W. J., & Quireza, C. 1999, *A&A*, 345, 629
- Maciel, W. J., Costa, R. D. D., & Uchida, M. M. M. 2003, *A&A*, 397, 667
- Magrini, L., Leisy, P., Corradi, R. L. M., et al. 2005, *A&A*, 443, 115
- Magrini, L., Corbelli, E., & Galli, D. 2007, *A&A*, 470, 843
- Magrini, L., & Gonçalves, D. R. 2009, *MNRAS*, 398, 280
- Magrini, L., Sestito, P., Randich, S., & Galli, D. 2009a, *A&A*, 494, 95
- Magrini, L., Stanghellini, L., & Villaver, E. 2009b, *ApJ*, 696, 729
- Magrini, L., Stanghellini, L., Corbelli, E., Galli, D., & Villaver, E. 2010, *A&A*, 512, A63
- Maraston, C. 1998, *MNRAS*, 300, 872
- Marigo, P. 2001, *A&A*, 370, 194
- Martin, P., & Roy, J.-R. 1994, *ApJ*, 424, 599
- McCall, M. L., Rybski, P. M., & Shields, G. A. 1985, *ApJS*, 57, 1
- McConnachie, A. W., Irwin, M. J., Ibata, R. A., et al. 2009, *Nature*, 461, 66
- Merrett, H. R., Merrifield, M. R., Douglas, N. G., et al. 2006, *MNRAS*, 369, 120
- Minchev, I., & Famaey, B. 2010, *ApJ*, 722, 112
- Minchev, I., Famaey, B., Combes, F., et al. 2011, *A&A*, 527, A147
- Minchev, I., Chiappini, C., & Martig, M. 2014, *A&A*, 572, A92
- Mollá, M., & Díaz, A. I. 2005, *MNRAS*, 358, 521
- Osterbrock, D. E., & Ferland, G. J. 2006, *Astrophysics of gaseous nebulae and active galactic nuclei*, 2nd ed. by D.E. Osterbrock and G.J. Ferland. Sausalito, CA: University Science Books, 2006,
- Pagal, B. E. J., & Edmunds, M. G. 1981, *ARA&A*, 19, 77

- Patterson, M. T., Walterbos, R. A. M., Kennicutt, R. C., Chiappini, C., & Thilker, D. A. 2012, *MNRAS*, 422, 401
- Pedicelli, S., Bono, G., Lemasle, B., et al. 2009, *A&A*, 504, 81
- Peimbert, M., & Serrano, A. 1980, *Rev. Mexicana Astron. Astrofis.*, 5, 9
- Peimbert, M., Storey, P. J., & Torres-Peimbert, S. 1993, *ApJ*, 414, 626
- Peña, M., Stasińska, G., & Richer, M. G. 2007, *A&A*, 476, 745
- Peng, E. W., Ford, H. C., & Freeman, K. C. 2004, *ApJ*, 602, 685
- Perinotto, M., Morbidelli, L., & Scatarzi, A. 2004, *MNRAS*, 349, 793
- Pilkington, K., Gibson, B. K., Brook, C. B., et al. 2012a, *MNRAS*, 425, 969
- Pilkington, K., Few, C. G., Gibson, B. K., et al. 2012b, *A&A*, 540, A56
- Pilyugin, L. S., & Mattsson, L. 2011, *MNRAS*, 412, 1145
- Pilyugin, L. S., Grebel, E. K., & Kniazev, A. Y. 2014, *AJ*, 147, 131
- Putman, M. E., Peek, J. E. G., Muratov, A., et al. 2009, *ApJ*, 703, 1486
- Quillen, A. C., Minchev, I., Bland-Hawthorn, J., & Haywood, M. 2009, *MNRAS*, 397, 1599
- Richer, M. G., & McCall, M. L. 2008, *ApJ*, 684, 1190
- Roškar, R., Debattista, V. P., Quinn, T. R., Stinson, G. S., & Wadsley, J. 2008, *ApJ*, 684, L79
- Roy, J.-R. 1996, *IAU Colloq. 157: Barred Galaxies*, 91, 63
- Rudolph, A. L., Fich, M., Bell, G. R., et al. 2006, *ApJS*, 162, 346
- Rupke, D. S. N., Kewley, L. J., & Chien, L.-H. 2010, *ApJ*, 723, 1255
- Sánchez, S. F., Rosales-Ortega, F. F., Iglesias-Páramo, J., et al. 2014, *A&A*, 563, A49
- Sanders, N. E., Caldwell, N., McDowell, J., & Harding, P. 2012, *ApJ*, 758, 133
- Schönrich, R., & Binney, J. 2009, *MNRAS*, 396, 203
- Searle, L. 1971, *ApJ*, 168, 327
- Sellwood, J. A., & Binney, J. J. 2002, *MNRAS*, 336, 785
- Sestito, P., Bragaglia, A., Randich, S., et al. 2006, *A&A*, 458, 121
- Stanghellini, L., & Haywood, M. 2010, *ApJ*, 714, 1096
- Stanghellini, L., Magrini, L., Villaver, E., & Galli, D. 2010, *A&A*, 521, A3
- Stanghellini, L., Magrini, L., Casasola, V., & Villaver, E. 2014, *A&A*, 567, A88
- Stanghellini, L., Magrini, L., & Casasola, V. 2015, arXiv:1508.02754
- Stasińska, G., Peña, M., Bresolin, F., & Tsamis, Y. G. 2013, *A&A*, 552, A12
- Stinson, G. S., Bailin, J., Couchman, H., et al. 2010, *MNRAS*, 408, 812
- Stinson, G. S., Brook, C., Macciò, A. V., et al. 2013, *MNRAS*, 428, 129
- Teuben, P. J. 2002, *discs of Galaxies: Kinematics, Dynamics and Perturbations*, 275, 217
- Tsamis, Y. G., Barlow, M. J., Liu, X.-W., Storey, P. J., & Danziger, I. J. 2004, *MNRAS*, 353, 953
- Tully, R. B., Courtois, H. M., Dolphin, A. E., et al. 2013, *AJ*, 146, 86
- van Zee, L., Skillman, E. D., & Haynes, M. P. 2006, *ApJ*, 637, 269
- Vila-Costas, M. B., & Edmunds, M. G. 1992, *MNRAS*, 259, 121
- Vilchez, J. M., & Esteban, C. 1996, *MNRAS*, 280, 720
- Werk, J. K., Putman, M. E., Meurer, G. R., & Santiago-Figueroa, N. 2011, *ApJ*, 735, 71
- Wong, T., Blitz, L., & Bosma, A. 2004, *ApJ*, 605, 183
- Woosley, S. E., & Weaver, T. A. 1995, *ApJS*, 101, 181
- Yong, D., Carney, B. W., Teixeira de Almeida, M. L., & Pohl, B. L. 2006, *AJ*, 131, 2256
- Yuan, T.-T., Kewley, L. J., Swinbank, A. M., Richard, J., & Livermore, R. C. 2011, *ApJ*, 732, L14
- Yun, M. S., Ho, P. T. P., & Lo, K. Y. 1994, *Nature*, 372, 530
- Zaritsky, D., Kennicutt, R. C., Jr., & Huchra, J. P. 1994, *ApJ*, 420, 87
- Zurita, A., & Bresolin, F. 2012, *MNRAS*, 427, 1463

## **Appendix A: Circular model fit of M31**

In this appendix we show the circular model fit for all the elliptical bins in M31 as performed in Section 4.2.

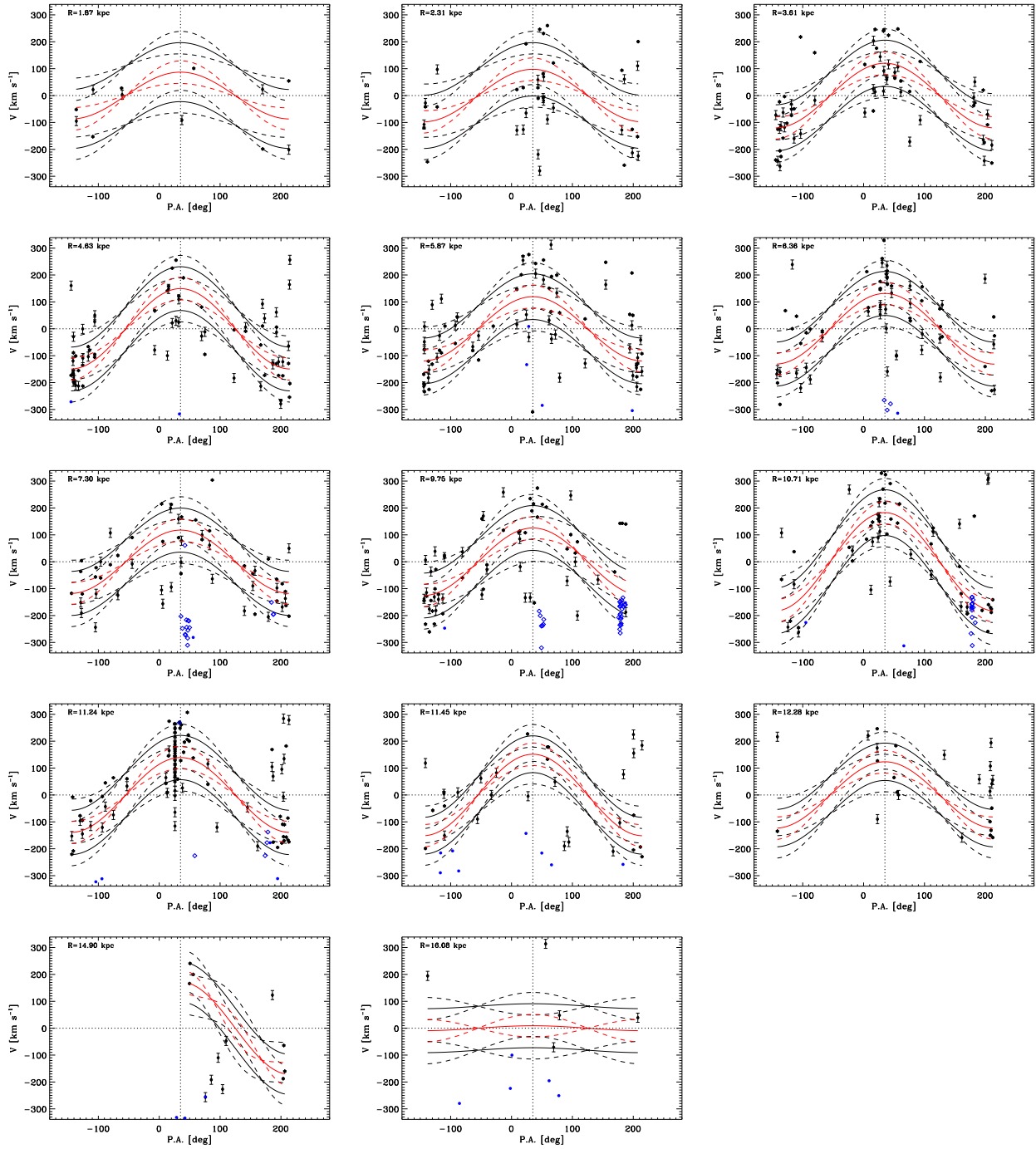


Fig. A.1. Same as Fig.4, but for the remaining elliptical bins of M31.